

# **Modal analysis of broadband acoustic receptions at 3515 km range in the North Pacific using short-time Fourier techniques**

**Kathleen E. Wage, Arthur B. Baggeroer, and James C. Preisig**

February 2003

*Journal of the Acoustical Society of America*, vol. 113(2), pp. 801-817.

# Modal analysis of broadband acoustic receptions at 3515-km range in the North Pacific using short-time Fourier techniques

Kathleen E. Wage<sup>a)</sup>

*Department of Electrical and Computer Engineering, George Mason University, Fairfax, Virginia 22030*

Arthur B. Baggeroer

*Departments of Ocean and Electrical Engineering, Massachusetts Institute of Technology, Cambridge, Massachusetts 02139*

James C. Preisig

*Department of Applied Ocean Physics and Engineering, Woods Hole Oceanographic Institution, Woods Hole, Massachusetts 02543*

(Received 3 May 2001; revised 3 September 2002; accepted 23 September 2002)

In 1995–1996 the Acoustic Thermometry of Ocean Climate (ATOC) experiment provided an opportunity to study long-range broadband transmissions over a series of months using mode-resolving vertical arrays. A 75-Hz source off the California coast transmitted broadband pulses to receiving arrays in the North Pacific, located at ranges of 3515 and 5171 km. This paper develops a short-time Fourier transform (STFT) processor for estimating the signals propagating in the lowest modes of the ocean waveguide and applies it to analyze data from the ATOC experiment. The STFT provides a convenient framework for examining processing issues associated with broadband signals. In particular, this paper discusses the required frequency resolution for mode estimation, analyzes the broadband performance of two standard modal beamforming algorithms, and explores the time/frequency tradeoffs inherent in broadband mode processing. Short-time Fourier analysis of the ATOC receptions at 3515 km reveals a complicated arrival structure in modes 1–10. This structure is characterized by frequency-selective fading and a high degree of temporal variability. At this range the first ten modes have equal average powers, and the magnitude-squared coherence between the modes is effectively zero. The coherence times of the peaks in the STFT mode estimates are on the order of 5.5 min. An analysis of mean arrival times yields modal dispersion curves and indicates that there are statistically significant shifts in travel time over 5 months of ATOC transmissions. © 2003 Acoustical Society of America.

[DOI: 10.1121/1.1530615]

PACS numbers: 43.30.Qd, 43.30.Re, 43.30.Bp, 43.60.Gk [DLB]

## I. INTRODUCTION

In deep water, the lowest-order acoustic normal modes are associated with the most energetic late arrivals at long range. Numerous authors, notably Munk and Wunsch,<sup>1</sup> have suggested using these arrivals in applications such as tomography and matched field processing. Using mode signals as observables requires the ability to associate a mode arrival with a particular path or section of the water column. In range-invariant environments, this problem is trivial because the modes propagate independently without exchanging energy, i.e., an arrival in mode 1 is known to have traversed the entire path in mode 1. For ranges on the order of megameters, however, inhomogeneities such as internal waves cause significant coupling of energy among the modes, resulting in complicated arrival patterns that are difficult to interpret. To date, tomographers have primarily relied on the earlier-arriving wavefronts, rather than the low-mode signals, in long-range experiments. Internal-wave-induced fluctuations associated with the rays can be studied within the context of

an existing theory,<sup>2</sup> whereas no comparable framework exists for the modes. Theoretical<sup>3,4</sup> and empirical<sup>5,6</sup> investigations of the long range propagation of modes through internal waves have yielded interesting results, but there have been few opportunities to relate them to experimental measurements of the mode arrival structure.

In 1995–1996 the Acoustic Thermometry of Ocean Climate (ATOC) experiment provided the first opportunity to observe broadband receptions over a period of months using mode-resolving vertical line arrays (VLAs). Two VLAs were part of a large network that also included U.S. Navy Sound Surveillance System (SOSUS) arrays.<sup>7</sup> Figure 1 shows paths from the bottom-mounted ATOC source on Pioneer Seamount to the two VLAs, located near Hawaii and Kiritimati (Christmas Island). Ranges to these arrays were 3515 and 5171 km, respectively. Each of the vertical arrays had 40 elements and spanned an aperture of 1400 m, providing adequate sampling of the first ten modes of the local environment. The source transmitted phase-encoded pseudo-random sequences with a center frequency of 75 Hz and bandwidth of 37.5 Hz. Transmissions occurred at 4-h intervals during periods set by the ATOC Marine Mammal Research Program.

<sup>a)</sup>Formerly at Department of Electrical Engineering and Computer Science, Massachusetts Institute of Technology, and Department of Applied Ocean Physics and Engineering, Woods Hole Oceanographic Institution.

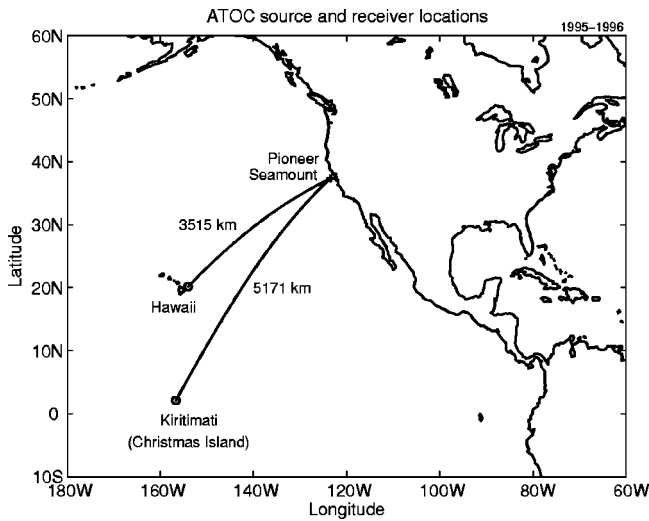


FIG. 1. ATOC source and vertical line array receivers.

This paper develops a short-time Fourier transform (STFT) method for estimating broadband signals propagating in the lowest modes of the deep water channel and analyzes receptions from the ATOC VLA at Hawaii using this approach. Since the modes are a frequency-dependent basis, broadband mode estimation requires separating the signal into frequency bins and using narrow-band mode filtering for each bin. Typically, researchers have implemented the required frequency decomposition using either a single long Fourier transform or a set of bandpass filters. These approaches are both special cases of the short-time Fourier transform. The STFT provides a convenient framework for exploring the time-frequency resolution tradeoffs that have not been addressed in previous work.

Short-time Fourier analysis of the Hawaii data set provides a detailed characterization of the low mode arrival structure at megameter range. In particular this paper quantifies the coherence of the first ten modes, estimates average dispersion curves, and examines trends in arrival time over the course of 5 months of ATOC transmissions.

The rest of the article is organized as follows. The next section reviews relevant aspects of long-range mode propagation, using simulations of the Pioneer–Hawaii path to illustrate the impact of internal waves on the mode arrivals. Section III reviews the broadband mode estimation problem and highlights the important issues associated with estimating broadband signals. Following that, Sec. IV presents a short-time Fourier framework for broadband mode estimation. Section V describes the results of the STFT analysis of the Hawaii data set. A summary concludes the paper.

## II. LONG-RANGE MODE PROPAGATION

Normal modes are the eigenfunctions of the ocean waveguide, derived from the frequency domain acoustic wave (Helmholtz) equation.<sup>8</sup> For a given environment and frequency, the  $m$ th mode is characterized by a horizontal wavenumber  $k_m$ , which defines its phase and group velocity, and a modeshape  $\phi_m$ , which defines its vertical structure.

The modes are an orthonormal basis for narrowband signals, thus the acoustic pressure at frequency  $\Omega$ , range  $r$ , and depth  $z$  can be represented as the weighted sum

$$p(r, z, \Omega) = \sum_m a_m(r, \Omega) \phi_m(r, z, \Omega), \quad (1)$$

where  $a_m$  is the frequency-dependent coefficient for mode  $m$ . From a simple input/output viewpoint, the underwater channel transforms the mode coefficients at the source into a set of coefficients at the receiver. In an adiabatic waveguide, the modes propagate independently without exchanging energy. For typical deep water channels, the low modes travel slowest since they represent energy trapped around the sound speed minimum. In addition, modal group velocities in these channels usually decrease with frequency.

When the medium is nonadiabatic, the modes exchange energy as they propagate. Range-dependent waveguides are often modeled as a cascade of range-independent segments, with the boundary conditions at the segment interfaces determining the mode coupling coefficients. Assuming that an environment is only weakly range-dependent, the adiabatic approximation simplifies the modeling problem by neglecting the coupling terms. Under this assumption, each propagating mode adapts with range (changes shape and wavenumber), but does not transfer energy into other modes. The validity of the adiabatic approximation is related to the nature of the inhomogeneities in the medium, and Desaubies concluded that its accuracy depends strongly on frequency, mode number, range and the acoustic quantity of interest, e.g., intensity, phase, travel time.<sup>9,10</sup>

Sound speed fluctuations due to internal waves are the dominant source of mode coupling in long-range propagation scenarios. To understand the impact of internal waves on the mode arrivals, consider two simulations for the 3515 km California–Hawaii path of the ATOC experiment. Figure 2 shows the results of a broadband parabolic equation (PE) simulation through a deterministic, range-varying model of the environment. This model was defined using sound speed profiles derived from the Levitus winter climatology<sup>11,12</sup> and bathymetry from the ETOPO-5<sup>13</sup> topography database.<sup>14</sup> The top plot in Fig. 2 is the synthesized pressure time series at the Hawaii array location, generated using the RAM PE code.<sup>15</sup> Spatial patterns associated with individual mode arrivals are evident in the pressure field, e.g., modes 2 and 3 (mode 1 is not strongly excited in this simulation). The figure beneath the pressure plot is the modal time series obtained by projecting the field (finely sampled in depth) onto the mode functions at the receiver. Note that the modes arrive in order from highest to lowest, as is consistent with deep water dispersion. Constructive interference of the higher modes results in the planewave (ray) arrivals in the early part of the reception.

Figure 3 illustrates how the results change when internal waves are present. For this simulation, the background sound speed profiles were perturbed by internal wave fluctuations at  $\frac{1}{2}$  Garrett-Munk strength, computed using the method of Colosi and Brown.<sup>16</sup> Instead of a single, dispersive arrival in each mode, there are multiple arrivals. This “modal multi-

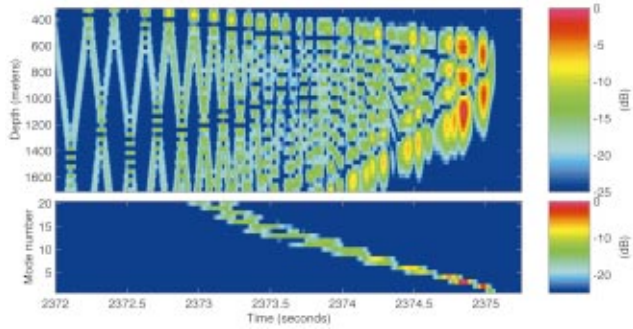


FIG. 2. Deterministic, range-varying simulation for California-ATOC path. Top panel shows the synthesized pressure time series,  $20 \log_{10} |p(t)|$ ; bottom panel shows the corresponding time series,  $20 \log_{10} |a(t)|$ , for the first 20 modes.

path” creates the more complicated interference patterns seen in the pressure time series.

From a theoretical standpoint, the effects of internal waves on long-range sound propagation are not fully understood. As indicated in the introduction, most previous work focused on the ray arrivals because they are amenable to analysis via a geometrical optics approximation. The monograph by Flatte *et al.* summarizes the path integral theory that predicts the fluctuations and coherence of resolved rays.<sup>2</sup> While there is no comparable theory for predicting the behavior of the mode arrivals, several authors have addressed aspects of the mode propagation problem. Some of the key results are described below.

In two seminal papers Dozier and Tappert derived modal intensity statistics for narrow-band signals in the presence of internal waves.<sup>3,6</sup> Their theory and numerical simulations showed that internal-wave-induced scattering eventually results in an equipartition of energy among the modes. The derivation of this result depends on several simplifying assumptions, including one that says there is no loss of energy into the bottom.

In one of the few studies of long-range experimental data, Colosi *et al.* compared pressure measurements from the 1000-km SLICE89 experiment to broadband PE simulations.<sup>17</sup> Their results showed that the broadening of the transmission finale in the data is attributable to the exchange of energy among the modes, caused by internal waves. In a later paper Colosi and Flatte explored the subject of mode coupling via internal waves using PE simulations designed to model certain aspects of the ATOC experiment.<sup>5</sup> They demonstrated the strong nonadiabatic character of propagation through these random fields and quantified the travel-time bias/spread and intensity fluctuations for the modes. A recent review article by Colosi *et al.* indicates that internal-wave-induced mode coupling is a major factor at 75 Hz, but may be significantly reduced at lower frequencies, e.g., 28 Hz.<sup>18</sup> Several papers have examined the degradation of mode coherence by internal waves concentrating on the implications for various signal processing methods, e.g., matched filtering,<sup>19</sup> horizontal array beamforming,<sup>20,21</sup> and vertical array beamforming.<sup>22</sup> Sazontov developed an approximate analytic method for computing the modal cross-coherences,<sup>23</sup> and Gorodetskaya *et al.* applied this technique to the study of

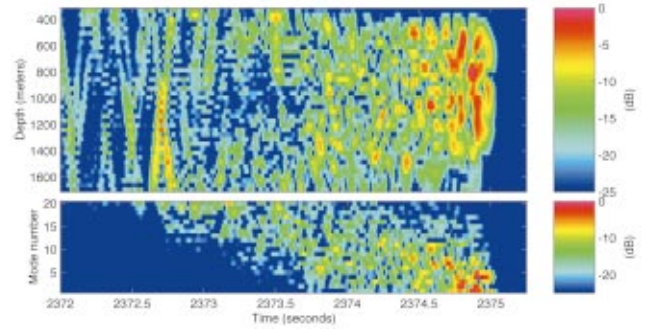


FIG. 3. Simulation for California-Hawaii environment perturbed by internal waves ( $\frac{1}{2}$  GM level). Top plot: pressure time series,  $20 \log_{10} |p(t)|$ ; bottom plot: modal time series,  $20 \log_{10} |a(t)|$ .

horizontal and vertical array gain limitations due to internal wave fluctuations.<sup>4</sup> These approximate expressions for coherence have not yet been validated by experimental data.

The ATOC experiment provided a significant opportunity to learn more about mode propagation out to megameter ranges. This paper examines the mode arrivals in the Hawaii data set, focusing in particular on the broadband characteristics and temporal stability of these signals. The following section reviews the problem of estimating mode arrivals using vertical arrays, specifically highlighting the issues associated with using broadband signals.

### III. BROADBAND MODE ESTIMATION PROBLEM

In many experiments, including ATOC, the low-order modes are not temporally resolvable, meaning that a vertical array is required to separate the mode signals based on their spatial characteristics.<sup>24</sup> An array measures the sum of modes (associated with the signal) plus noise, i.e., in vector notation,

$$\mathbf{p}[r, \Omega] = \Phi[r, \Omega] \mathbf{a}[r, \Omega] + \mathbf{n}[\Omega]. \quad (2)$$

$\Phi$  is the matrix of sampled modeshapes,  $\mathbf{a}$  is the vector of mode amplitudes, and  $\mathbf{n}$  is the vector of observation noise. For a broadband source, the measurement is a vector time series

$$\Psi(r, t) = \int_{\Omega} (\Phi[r, \Omega] \mathbf{a}[r, \Omega] + \mathbf{n}[\Omega]) e^{j\Omega t} d\Omega. \quad (3)$$

The objective of mode processing is to estimate the vector of mode coefficients ( $\mathbf{a}[r, \Omega]$ ), or equivalently to estimate the corresponding mode time series. Section III A discusses two important design criteria for mode filters, and Sec. III B reviews previous work on this topic.

#### A. Design issues

The most important issue to consider in broadband mode estimation is the frequency dependence of the modeshapes. As an example, Fig. 4 illustrates how the first ten modes at the ATOC Hawaii array vary as a function of frequency. A comparison of the modeshapes at 60 and 90 Hz indicates that they change significantly over the 30-Hz interval (approximate bandwidth of the ATOC source). Obviously, any spatial

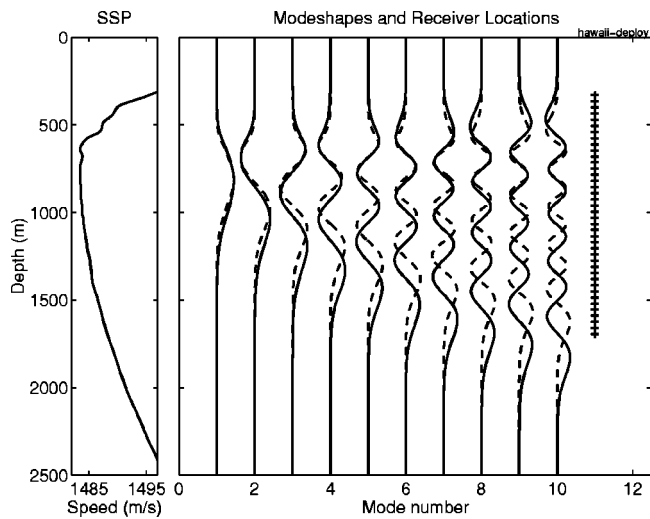


FIG. 4. Measured sound speed profile and first ten modeshapes (at 60 and 90 Hz) for the ATOC Hawaii environment. Water depth at array location is 5426 m; only the top 2500 m are shown in the plot. The '+'s indicate nominal sensor positions for the 40-element VLA.

processing that requires a replica of the sampled mode shape must be done on a set of subbands to avoid mismatch problems. In general the maximum width of these bands is determined by the environment and center frequency. Since bandpass filtering smears signals in time, the broadband mode filter design process inherently involves time and frequency resolution tradeoffs.

Separating the signal into subbands reduces mode estimation to a classical linear inverse problem.<sup>25,26</sup> The key issue to consider in solving each of the narrowband problems is the spatial sampling of the modeshapes by the array since that determines how well the processor can resolve a mode and reject noise.<sup>27</sup> From the point of view of estimating a single mode, there are two types of noise to consider: structured interference from signals propagating in other modes and uncorrelated measurement noise (due to ships, etc.). Based on Fig. 3, it is reasonable to assume that time-windowing can be used to limit the structured interference from the earliest ray arrivals (corresponding to high order modes), since they do not overlap in time with the lowest modes.

## B. Previous work

Most previous research focused on experimental settings where a narrowband assumption is valid, meaning that either the source is continuous wave (CW) or the variations in the mode functions across the source band are negligible. Two basic types of mode filters have been developed for narrowband signals: the matched filter (MF)<sup>28,29</sup> and the pseudo-inverse (PI) filter.<sup>30</sup> The performance of these filters is well understood. The matched filter (sometimes called the sampled modeshapes filter) has the advantage of a simple and stable implementation, but it does not guarantee that energy from one mode will not leak into an adjacent mode. On the other hand, the PI filter ensures good modal crosstalk rejection at the expense of increased noise sensitivity. Headrick *et al.* provide a useful discussion of the matched filter in

the context of the shallow water SWARM 95 internal wave scattering experiment.<sup>31</sup> They assess the variability in cross-mode rejection due to array tilt and temporal fluctuations of the modeshapes. SWARM 95 used a 400-Hz broadband source (100-Hz bandwidth), but the authors conclude that a narrowband mode filter is sufficient because the modes do not change significantly across the source band.

For some broadband experiments, variations in the modeshapes and wavenumbers as a function of frequency are too large to ignore. The standard solution to the broadband problem consists of separating the signal into frequency bins using a single long Fourier transform, doing narrow-band mode processing for each bin, and obtaining a time series via an inverse transform.<sup>32–34</sup> Sutton *et al.*<sup>35</sup> and Heaney and Kuperman<sup>36</sup> suggest using a windowed Fourier transform to compute the mode estimates. Others propose using bandpass filters to process the data in bands where the modeshapes may be assumed constant.<sup>37</sup> None of these studies discuss how the frequency resolution (determined by the length of the window or the width of the bandpass filter) affects the mode estimates.

This paper generalizes the previous approaches by using a short-time Fourier transform (STFT) framework to analyze the time/frequency tradeoffs inherent in broadband mode estimation. An STFT-based processor separates the signal into a set of subbands and estimates the modal time series in each band. The results are time-varying mode spectra that can be used to examine the frequency-dependent structure in the signals, e.g., to quantify dispersion or frequency-selective fading. An important advantage of the STFT approach is that it provides a method of analyzing the characteristics of individual multipath arrivals within a mode, provided that short enough time windows can be used in the processing. This facilitates the search for frequency-coherent mode arrivals. The extent of the modeshape variations with frequency determines the maximum temporal resolution that is attainable with a mode processor for a particular environment.

The following section develops the short-time Fourier mode processing framework, explores important time/frequency resolution issues, and selects the processing parameters for the ATOC Hawaii experimental dataset.

## IV. SHORT-TIME FOURIER MODE PROCESSING FRAMEWORK

The short-time Fourier transform is a standard signal processing technique for examining the characteristics of transient or time-varying signals.<sup>38,39</sup> STFT analysis consists of computing discrete Fourier transforms for a sequence of finite-length data segments. There are two equally valid interpretations of the resulting time-dependent spectrum: (1) as the output of a filterbank or (2) as the output of a windowed Fourier transform operation. This section relies on the first interpretation to describe the application of STFT techniques to broadband mode estimation. The discussion is organized as follows. Section IV A provides an overview of the short-time Fourier mode processor. Following that, Secs. IV B and IV C discuss narrowband mode filters and their broadband

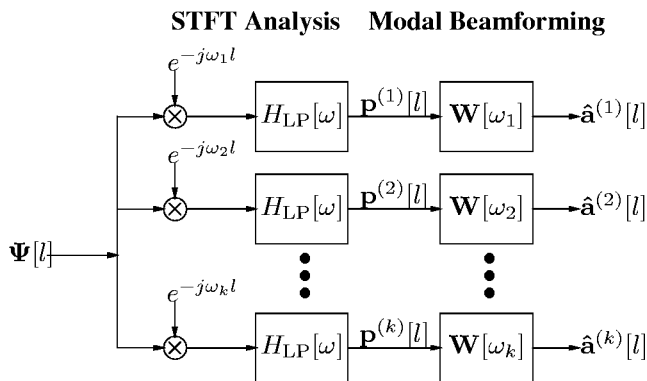


FIG. 5. Block diagram of STFT-based mode processor.

performance characteristics, respectively. Finally, Sec. IV D illustrates the properties of short-time mode estimates using an adiabatic propagation example.

### A. Overview

In STFT-based mode analysis, the processor separates the received pressure into a set of subbands and computes mode estimates for each subband. Figure 5 illustrates these steps and introduces some notation. The input to the filterbank is  $\Psi[l]$ , a sampled vector time series from an  $N$ -element receiving array. As shown, the filtering operation consists of complex demodulation followed by lowpass filtering; this is equivalent to bandpass filtering followed by demodulation. The result of the STFT analysis step is an  $N$ -point complex vector time series of pressures for each band:  $\mathbf{p}^{(k)}[l]$ , where  $k$  denotes the band (bin) number and  $l$  is the time index. After filtering, the processor computes a vector time series of mode coefficients for each band using a set of narrow-band modal beamformers. The result is an  $M$ -point vector  $\hat{\mathbf{a}}^{(k)}[l]$  containing the estimated short-time Fourier transform of the first  $M$  modes in the bin centered around  $\omega_k$ .<sup>40</sup>

Within the STFT framework, the length of the lowpass filter,  $H_{LP}[\omega]$ , determines the time and frequency resolution of the estimates. Long filters (equivalent to using long data windows for the Fourier transform) have good frequency resolution, implying that the required operating bandwidth for the modal beamformer  $\mathbf{W}[\omega_k]$  is small. The disadvantage of long filters is that they smear the arrivals in time. Short filters provide much better temporal resolution, but they have wider passbands, meaning that the processor may be more sensitive to the frequency-dependent variations of the modeshapes. In general  $H_{LP}$  can be any filter with a lowpass characteristic, but short-time Fourier analysis typically employs the same filters (windows) that are used in spectral estimation. Harris provides an extensive list of window functions in his classic paper.<sup>41</sup>

The STFT approach reduces the broadband estimation problem to a set of narrowband problems. Assuming that the modeshapes are constant over the band defined by the lowpass filter, the pressure measurement in the  $k$ th band becomes

$$\mathbf{p}^{(k)}[l] = \Phi[\omega_k] \mathbf{a}^{(k)}[l] + \mathbf{n}^{(k)}[l], \quad (4)$$

where  $\Phi[\omega_k]$  is the matrix of sampled modeshapes at the band's center frequency,  $\mathbf{a}^{(k)}$  is a vector of bandpass-filtered, time-varying mode coefficients, and  $\mathbf{n}^{(k)}$  is a noise vector. As noted above, estimating the mode amplitudes from the measured pressure is a classic inverse problem. This paper focuses on solutions of the form

$$\hat{\mathbf{a}}^{(k)}[l] = \mathbf{W}_k^H \mathbf{p}^{(k)}[l], \quad (5)$$

where  $\mathbf{W}_k^H$  is a matrix containing the deterministic, time-invariant spatial filter for the  $k$ th band (the superscript  $H$  denotes the conjugate transpose operator). Time- and data-adaptive solution methods could be incorporated into the STFT framework once more is known about the structure of mode signals at long ranges.

The next section briefly describes standard narrowband mode filters, and a subsequent section reviews their broadband performance.

### B. Narrow-band mode filters

As indicated in Sec. III B, the two standard solutions to the narrow-band mode estimation problem are the matched filter and the pseudo-inverse mode filter. There are several ways to derive these filters. The approach described below is based on optimizing array gain and provides a complementary perspective to the estimation theory derivation that is more common in the mode filtering literature (see Ref. 27 for a summary). An advantage to viewing mode filtering as a constrained optimization problem is that it emphasizes the inherent tradeoff between interference rejection and processor sensitivity.

Array gain represents the improvement in the signal-to-noise ratio (SNR) due to processing. It is typically defined as the ratio of the SNR at the output of a beamformer to the SNR at a single sensor. Since the signal and noise characteristics often vary across an array, the input SNR is taken to be an average (arithmetic or geometric) of the single-phone SNRs. In the case of modal beamforming, the signal levels vary from one sensor to another because the modeshapes are functions of depth. White noise gain,  $G_w$ , represents the gain of the processor when the noise is assumed to be spatially white. For the mode processing problem, the gain for mode  $m$  is defined as

$$G_w = N \frac{|\mathbf{w}_m^H \boldsymbol{\phi}_m|^2}{|\mathbf{w}_m|^2 |\boldsymbol{\phi}_m|^2}, \quad (6)$$

where  $\mathbf{w}_m$  is the weight vector (filter) and  $\boldsymbol{\phi}_m$  is the sampled modeshape vector for the  $m$ th mode. Equation (6) assumes that the input SNR is equal to the arithmetic average SNR across the array. Application of the Schwartz inequality shows that the maximum value of the white noise gain is  $N$ , the number of sensors in the array. In addition to describing the noise response,  $G_w$  provides a useful measure of the sensitivity of the processor to mismatch, as discussed by Cox *et al.*<sup>42</sup>

The matched filter (MF) results from choosing the weight vector for mode  $m$  that maximizes white noise gain while maintaining a unit gain in the desired mode. Maximizing  $G_w$  subject to a unity gain constraint is mathematically

equivalent to minimizing the squared length of the weight vector subject to the same gain constraint, thus the optimization problem becomes

$$\min |\mathbf{w}_m|^2 \text{ subject to } \mathbf{w}_m^H \boldsymbol{\phi}_m = 1. \quad (7)$$

Standard optimization techniques yield the following solution,

$$\mathbf{w}_m^H = \frac{1}{|\boldsymbol{\phi}_m|^2} \boldsymbol{\phi}_m^H, \quad (8)$$

or in terms of the weight matrix for  $M$  modes

$$\mathbf{W}^H = \begin{bmatrix} \frac{1}{|\boldsymbol{\phi}_1|^2} & & 0 \\ & \ddots & \\ 0 & & \frac{1}{|\boldsymbol{\phi}_M|^2} \end{bmatrix} \mathbf{E}^H, \quad (9)$$

where  $\mathbf{E}$  is the sampled modeshape matrix containing the  $M$  desired modes, i.e., the first  $M$  columns of  $\boldsymbol{\Phi}$ . The matched filter is optimal in the sense that it achieves the maximum white noise gain ( $G_{w-MF} = N$ ), but it does not explicitly prevent the signal in one mode from leaking into another. Instead, it relies on the orthogonality of the modes to separate them. It is important to note that while the modeshapes are orthogonal functions of the continuous depth variable  $z$ , the sampled modeshape vectors are not guaranteed to have this property.

The pseudo-inverse (PI) filter results from constraining mode leakage by placing nulls in the modal beampattern at the locations of a set of interfering modes. In this case, the optimization problem consists of maximizing the white noise gain (minimizing the weight vector length) subject to multiple constraints, i.e.,

$$\min |\mathbf{w}_m|^2 \text{ subject to } \begin{cases} \mathbf{w}_m^H \boldsymbol{\phi}_m = 1, \\ \mathbf{w}_m^H \boldsymbol{\phi}_{n \neq m} = 0, \quad 1 \leq n \leq M. \end{cases} \quad (10)$$

It is useful to rewrite the problem as

$$\min |\mathbf{w}_m|^2 \text{ subject to } \mathbf{w}_m^H \mathbf{E} = \mathbf{c}_m^T, \quad (11)$$

where  $\mathbf{E}$  contains the first  $M$  columns of the sampled modeshape matrix and  $\mathbf{c}_m$  is an  $M$ -point column vector with a one in the  $m$ th position and zeros everywhere else. When the sampled modeshape matrix is full rank, standard optimization techniques yield the following solution for the weight vector

$$\mathbf{w}_m^H = \mathbf{c}_m^T (\mathbf{E}^H \mathbf{E})^{-1} \mathbf{E}^H. \quad (12)$$

Equation (12) corresponds to one row of the pseudo-inverse of the sampled modeshapes matrix containing the first  $M$  modes, thus  $\mathbf{W}^H$  is simply

$$\mathbf{W}^H = (\mathbf{E}^H \mathbf{E})^{-1} \mathbf{E}^H. \quad (13)$$

Assuming that  $\mathbf{E}$  has full rank, the null constraints in Eq. (11) are met exactly and the processor for mode  $m$  rejects the  $M - 1$  other modes included in the pseudo-inverse. In terms of interference rejection, the PI filter guarantees better performance than the matched filter, but this improvement may

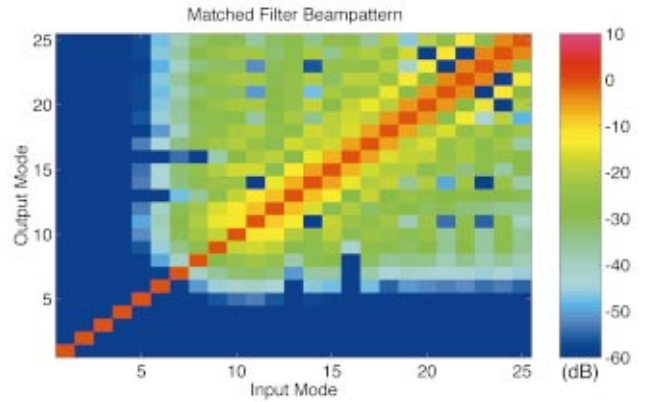


FIG. 6. Matched filter beampattern (75 Hz) for the 40-element ATOC VLA at Hawaii.

come at the expense of increased sensitivity to noise or other perturbations. Consider the white noise gain for the  $m$ th mode:

$$G_{w-PI} = \frac{N}{|\boldsymbol{\phi}_m|^2} \cdot \frac{1}{\mathbf{c}_m^T (\mathbf{E}^H \mathbf{E})^{-1} \mathbf{c}_m}. \quad (14)$$

Recalling that  $\mathbf{c}_m^T \mathbf{c}_m$  is equal to unity, the second term in Eq. (14) can be written as the inverse of a Rayleigh quotient<sup>43</sup> and is therefore known to be bounded by the squared singular values of the sampled modeshape matrix, i.e.,

$$\sigma_{\min}^2 \leq \frac{\mathbf{c}_m^T \mathbf{c}_m}{\mathbf{c}_m^T (\mathbf{E}^H \mathbf{E})^{-1} \mathbf{c}_m} \leq \sigma_{\max}^2, \quad (15)$$

where  $\sigma_{\min}$  and  $\sigma_{\max}$  are the minimum and maximum singular values of  $\mathbf{E}$ , respectively. If the sampled modeshapes are orthogonal,  $\mathbf{E}^H \mathbf{E}$  is a diagonal matrix where the  $m$ th term on the diagonal is equal to  $|\boldsymbol{\phi}_m|^2$ . In this case the quotient in Eq. (15) reduces to  $|\boldsymbol{\phi}_m|^2$ , and the white noise gain is equal to the optimal value of  $N$ . On the other hand, if the array does not adequately sample the modes, the modeshape vectors are

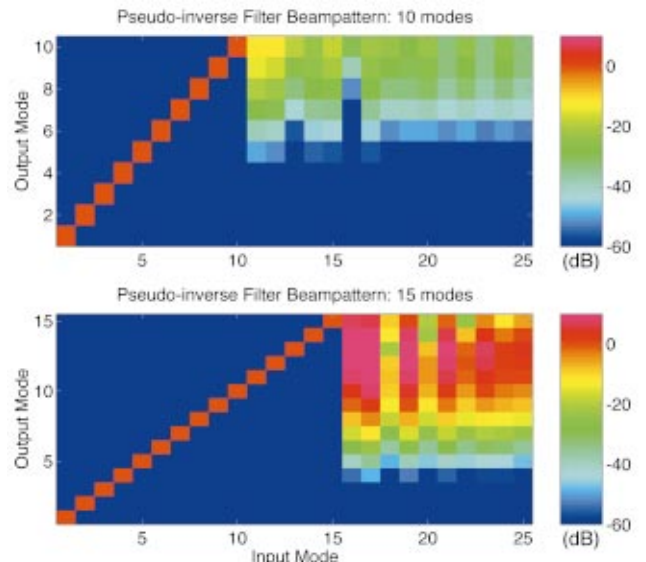


FIG. 7. Comparison of 10- and 15-mode pseudo-inverse filter beampatterns (75 Hz) for the ATOC VLA at Hawaii.

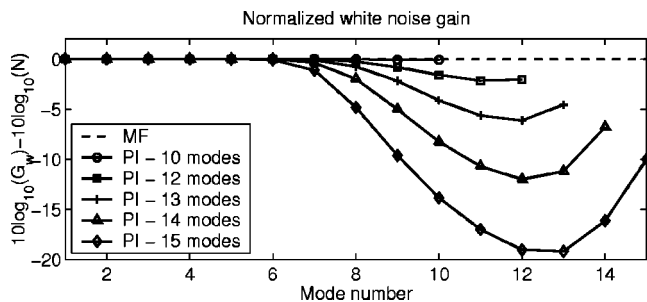


FIG. 8. Comparison of white noise gain for the matched filter and 10-, 12-, 13-, 14-, and 15-mode pseudo-inverse filters at 75 Hz for the ATOC Hawaii VLA.  $G_w$  is normalized by  $N$ , the maximum gain for an array with  $N$  hydrophones. Results are shown in dB.

not orthogonal and some singular values of  $\mathbf{E}$  may be very small. As one or more of the singular values approach zero, the white noise gain is substantially reduced and the pseudo-inverse becomes ill-conditioned. There are a number of standard techniques for mitigating problems with small singular values in the pseudo-inverse, e.g., diagonal loading<sup>44</sup> and elimination of small eigenvalues in the inverse.<sup>45</sup> These methods increase robustness at the expense of biasing the mode estimates. For the ATOC analysis we limit the number of modes in the pseudo-inverse rather than using one of these alternative approaches.

Beampatterns provide a useful illustration of the narrow-band performance of these two mode processors. In the context of mode filtering, the beampattern is defined as  $20 \log_{10}(\mathbf{W}^H \Phi)$ , where  $\mathbf{W}$  is the multidimensional mode filter and  $\Phi$  is the matrix of sampled modeshapes. The  $m$ th row of the beampattern matrix corresponds to the projection of the modes into the estimate for mode  $m$ .

For the matched filter, the beampattern corresponds to a normalized version of the sampled modeshape correlation matrix,  $\Phi^H \Phi$ . Figure 6 shows the matched filter beampattern for the first 25 modes at 75 Hz, using the 40-element ATOC VLA at Hawaii. This filter has excellent crosstalk rejection for modes up to 8; above 8 the sampled modeshapes are obviously correlated. As a result, energy from one mode leaks into estimates of adjacent modes. Performance of the matched filter in this environment degrades significantly for modes above 10, which is not surprising since the array was designed to spatially resolve the first 10 modes.

Figure 7 shows the 75-Hz beampatterns for two pseudo-inverse filters, designed for 10 modes and 15 modes, respectively. These plots confirm that the PI filter for mode  $m$  has nulls at the locations of all the other modes included in the estimate, resulting in the beampattern's diagonal structure. The beampatterns also illustrate how higher order modes (that are not included in the pseudo-inverse) project into the lower modes. As these plots show, the amount of crosstalk depends on the number of modes in the filter, i.e., the 10-mode filter is significantly better at rejecting energy from higher modes than the 15-mode filter. This is due to the fact that the amount of crosstalk is governed by the conditioning of the pseudo-inverse, which degrades as more modes are included.

Figure 8 demonstrates how adding constraints (i.e., additional modes) increases a filter's sensitivity to noise. The

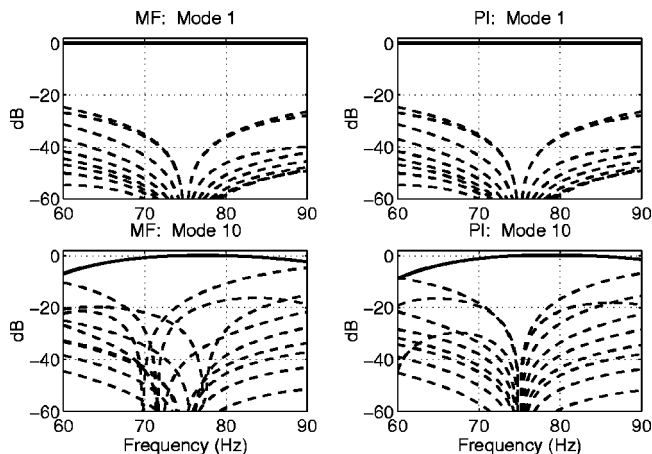


FIG. 9. Frequency-dependent beampatterns for the matched filter and 10-mode pseudo-inverse filter. The filters are designed for the 75-Hz bin using the ATOC Hawaii VLA modeshapes.

plot shows white noise gain as a function of mode number for the matched filter and five pseudo-inverse filters, designed for 10, 12, 13, 14, and 15 modes, respectively. Note that the results are normalized by  $N$ , the maximum possible white noise gain. The plot confirms that the matched filter achieves the optimal gain and also shows that the gain of the 10-mode pseudo-inverse filter is equivalent to the matched filter. Curves for the 12-, 13-, 14-, and 15-mode PI filters indicate that there is a significant loss in white noise gain as additional null constraints are added to the design. The reason is that modes above 10 are not adequately sampled by the 40-element ATOC VLA, therefore the smallest singular values of  $\mathbf{E}$  decrease dramatically as these modes are included.

### C. Broadband performance analysis

In designing a short-time Fourier mode processor, it is crucial to have a measure of how well a narrowband mode filter designed for particular frequency performs on the modes at neighboring frequencies. The operating bandwidth of the narrowband mode filters determines the required frequency resolution of the lowpass filter, which in turn defines the temporal resolution of the processor. This section addresses the broadband performance issues associated with the STFT approach by examining the frequency and noise responses of the MF and PI mode filters.

The frequency-dependent beampattern characterizes the frequency response of the STFT processor. For the  $k$ th bin, this beampattern is defined as  $20 \log_{10}(\mathbf{W}_k^H \Phi[\omega])$ , where  $\mathbf{W}_k$  is the narrow-band spatial filter designed with the modeshapes at the center frequency of the bin. Figure 9 shows the broadband beampatterns for modes 1 and 10, generated with MF and PI filters for the ATOC Hawaii VLA. The pseudo-inverse filter includes the first ten modes. Each of the spatial filters is designed for a center frequency of 75 Hz, and the results are shown for the 30 Hz ( $\pm 15$  Hz) band around that frequency. The solid lines in the plots represent the response in the desired mode and the dashed lines represent the crosstalk from neighboring modes (from 1 to 10) into the desired mode. As Fig. 9 indicates, both filters have a flat

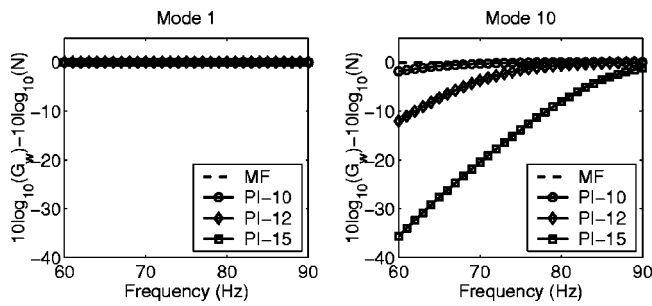


FIG. 10. White noise gain (normalized by  $N$ ) as a function of frequency for the matched filter and three different pseudo-inverse filters (for 10, 12, and 15 modes). Results are shown in dB.

response in mode 1, which is reasonable considering that the first mode's shape does not vary significantly with frequency (see Fig. 4). At 75 Hz there are nulls in the response of mode 1 to input from modes 2–10, but crosstalk increases substantially as  $\omega$  deviates from the design frequency. The plots for mode 10 indicate that frequency mismatch can affect the gain in the desired mode as well as the crosstalk rejection, e.g., the gain in mode 10 is down by 10 dB at 60 Hz. This is due to the significant changes in the shape of mode 10 as a function of frequency, illustrated in Fig. 4. As expected from the narrowband analysis of the previous section, the frequency-dependent beampattern shows that the MF beamformer does not prevent crosstalk at the center frequency in mode 10. In contrast the PI filter for mode 10 is constrained to have nulls at 75 Hz for modes 1–9. Figure 9 demonstrates that these constraints are not satisfied for frequencies other than the design frequency.

Based on the MF and PI beampatterns shown, frequency mismatch affects crosstalk rejection much more than it affects the response in the desired mode. Thus the allowable crosstalk defines the operating bandwidth of the mode filters. For example, to guarantee a maximum crosstalk level over the band of less than  $-20$  dB, the bandwidth of the ten-mode PI filter is  $\pm 2.5$  Hz. Using this criteria, the cutoff frequency of the lowpass filter ( $H_{LP}$ ) in the STFT processor for ATOC should be  $\pm 2.5$  Hz. In addition, since the crosstalk levels in Fig. 9 are increasing away from the center frequency, it is desirable for the temporal filter to have decreasing (rather than constant) sidelobes. To meet these specifications, the lowpass filter chosen for the ATOC data is a 0.4-s Hanning window, which has a  $-3$  dB bandwidth of  $\pm 2.5$  Hz and sidelobes that fall off at a rate of  $1/\omega^3$ . Recall from Sec. IV A that the temporal resolution of the processor is determined by the length of the lowpass filter. The Hanning window taper is such that it can begin to temporally resolve arrivals when they are farther apart than half its length, thus the resolution of the ATOC short-time Fourier processor is on the order of 0.2 s.

The pseudo-inverse filter clearly provides better crosstalk rejection than the matched filter, however it is subject to problems with the conditioning of the matrix inverse. As discussed in Sec. IV B, white noise gain is a convenient measure of processor sensitivity. Figure 10 shows the white noise gain, normalized by  $N$ , of the filters for modes 1 and 10 as a function of center frequency. Each of the plots have

TABLE I. Simulation parameters for the California–Hawaii adiabatic propagation example.

Source range	700 m
Center frequency	75 Hz
Pulse	triangular-windowed sinusoid
Pulse duration	0.11 s ( $\approx 30$ Hz bandwidth)
Receiver depth	3515.2 km
No. of receivers	40
Element spacing	35 m
Span	330–1695 m
Sample rate	300 Hz
Modes	No. included 40

four curves: one for the matched filter and three for different realizations of the pseudo-inverse filter that are designed for 10, 12, and 15 modes, respectively. For mode 1 all three pseudo-inverse filters achieve the optimal (matched filter) white noise gain of  $10 \log_{10}(N)$  regardless of frequency. The plot for mode 10 illustrates an important characteristic of the white noise gain for the higher-order modes: white noise gain decreases as frequency decreases. This is due to the fact that the modeshapes at lower frequencies occupy a greater portion of the water column (see Fig. 4), thus are not spanned as well by the array, resulting in a sampled mode-shape matrix with small singular values. Note that for the 10-mode PI filter white noise gain is almost constant across the 30-Hz band of interest.

Based on the discussion above, the pseudo-inverse filter for ten modes provides a better combination of noise gain and interference rejection than either the matched filter or PI filters designed for higher numbers of modes. The next section illustrates the characteristics of short-time Fourier mode estimates obtained by using the ten-mode PI filter to process a simulated reception on the ATOC array.

#### D. STFT processing example

Table I summarizes the parameters for an adiabatic simulation of propagation over the California–Hawaii path of the ATOC experiment. The environment contains a broadband point source at 700-m depth, located 3515.2 km away from a 40-element receiving array with 35-m spacing (identical to the ATOC VLAs). In this example, the source transmits a single windowed-sinusoidal pulse with approximately 30-Hz bandwidth, at a center frequency of 75 Hz. The time series for the receivers is synthesized from the first 40 modes,<sup>46</sup> using range-averaged wavenumbers calculated from Levitus winter climatology and range-varying bathymetry for the path. Figure 11 shows the received pressure field for the adiabatic simulation. At 3515.2-km range, the modes are dispersed enough that it is possible to identify individual modes in the pressure time series, e.g., mode 1 is the strong final arrival,<sup>47</sup> and mode 5 is associated with the five strong peaks lined up right after 2374.5 s.

Figure 11 also shows the corresponding short-time Fourier mode estimates, as a function of time and frequency, for modes 1, 5, and 10. The estimates were computed using processing parameters identical to those used on the ATOC data in the next section: a 0.4-s Hanning window lowpass

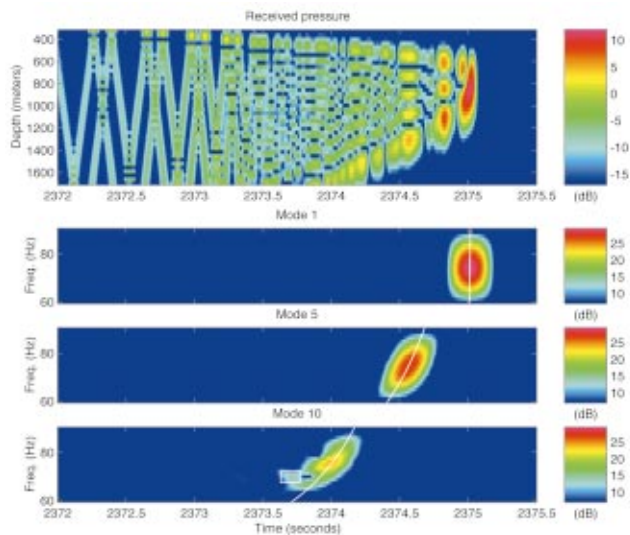


FIG. 11. STFT processing of adiabatic simulation of California–Hawaii path. Top plot is the synthesized pressure field on 40-element array. Bottom plots are the short-time Fourier estimates for modes 1, 5, and 10. White lines in the mode estimates represent the adiabatic arrival times. The white box indicates the components in the mode 10 signal that are due to crosstalk from modes 11 and 12.

filter and a ten-mode pseudo-inverse spatial filter. For this example the bin spacing of the STFT filterbank is 1.25 Hz. Since the lowpass filter has a bandwidth of approximately  $\pm 2.5$  Hz, neighboring bins are highly correlated. A 2.5-Hz bin spacing is all that is required to adequately represent the underlying signals filtered by the Hanning window. Oversampling by a factor of 2 in frequency improves the appearance of the plots, but does not affect the overall resolution of the processor. The solid white line in each plot corresponds to the mode arrival time computed using adiabatic group velocities.

These plots demonstrate that the STFT mode processor is working as expected. First, the arrivals in the estimated modal time series correctly line up with the appropriate peaks in the pressure time series and the adiabatic predictions. Second, the dispersion characteristics of each mode are visible in the output. Mode 1 shows all frequencies arriving at the same time, meaning it is undispersed, whereas modes 5 and 10 clearly show the lower frequencies arriving first, as expected in deep water. Third, with the exception of a small amount of crosstalk (indicated by the white box in the bottom plot) from modes 11 and 12 into earliest arrivals of mode 10, the STFT processor effectively filters out the higher-order modes. Note that this crosstalk is predicted by the beam pattern in Fig. 7. Finally, the temporal smearing caused by the 0.4-s low-pass filter is evident in the broader arrival peaks of the mode time series, as compared to the arrivals in the simulated VLA data.

## V. STFT ANALYSIS OF RECEPTIONS AT 3515 km

This section presents an analysis of the ATOC receptions on the Hawaii vertical line array using the short-time Fourier techniques described in Sec. IV. The discussion begins with an overview of the experimental data set, including a brief description of the source/receiver configuration and pre-

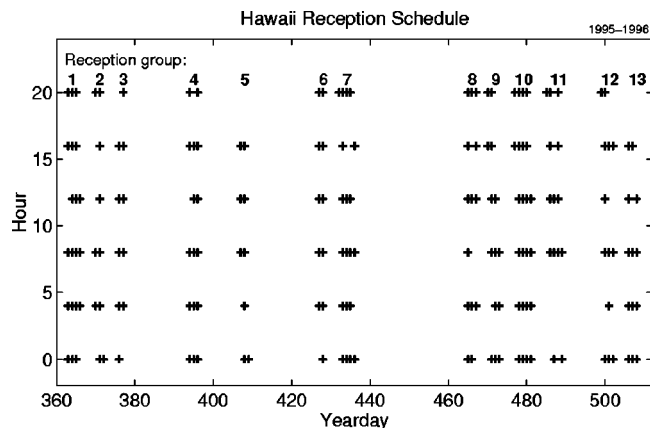


FIG. 12. ATOC transmission schedule through yearday 509. Crosses mark the time of each good reception; receptions with bad channels were eliminated from the data set. The line of numbers above the crosses indicates the division into 13 subgroups for postprocessing.

processing algorithms. Following that, Sec. V B describes the short-time Fourier mode estimates for the ATOC receptions and compares them to the results for simulated receptions. Sections V C and V D address the issues of mode coherence and temporal variability, respectively. Finally, Sec. V E discusses mode arrival time statistics and analyzes trends over the course of the experiment.

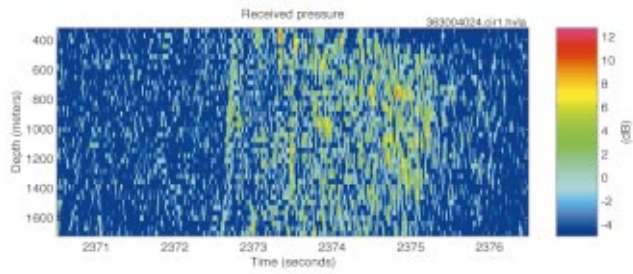
### A. ATOC Hawaii VLA data set

As noted in the Introduction, the ATOC experiment employed a bottom-mounted source at Pioneer Seamount (off California) and two vertical arrays, located near Hawaii and Kiritimati in the Northeastern Pacific. A paper by the ATOC Instrumentation Group provides a thorough description of the source and receiver hardware.<sup>48</sup> What follows is a brief review of the relevant details.

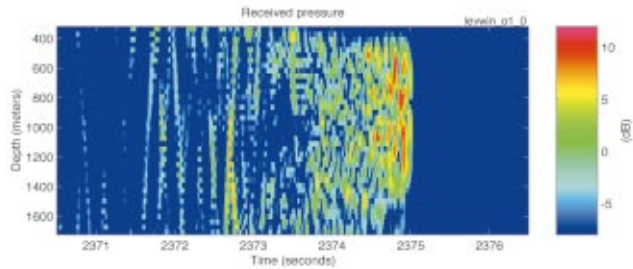
The source transmitted phase-encoded pseudo-random sequences at a center frequency of 75 Hz, with a  $-3$  dB bandwidth of 37.5 Hz. Each transmission consisted of 44 repetitions of the 27.28-s (1023 digits) *M*-sequence, corresponding to a transmission length of approximately 20 min. The source and the two VLAs were deployed in the fall of 1995, and regular transmissions began in December of that year. Over the course of the experiment, the source transmitted signals every 4 h during periods set by the ATOC Marine Mammal Research Program.

This paper describes the analysis of data recorded on the 40-element array near Hawaii, located at a range of 3515.2 km from the source. Figure 12 shows the schedule of reception times for this array from 28 December 1995 (yearday 362) to 23 May 1996 (yearday 509). Although the array was not recovered until August 1996, the deepest 20 hydrophones failed sometime after day 509. Since mode processing is much more difficult with only the shallow half of the array (due to inadequate sampling of the modeshapes), this study is limited to receptions recorded with the full array. There were 229 transmissions between yeardays 362 and 509. Forty-one of these were eliminated from the analysis due to incomplete or corrupted time series, leaving the 188 receptions shown in Fig. 12.

For each transmission, the 40-element array recorded the



(a) Reception at Hawaii VLA on yearday 363.



(b) PE simulation with internal waves at 1/2 GM strength.

FIG. 13. Comparison of experimental and simulated receptions for the Hawaii VLA. (a) Reception at Hawaii VLA on yearday 363. (b) PE simulation with internal waves at  $\frac{1}{2}$  GM strength.

received signal on each hydrophone, averaged over four periods of the pseudo-random sequence. Ten such averages, spanning an 18.2-min interval, were recorded for each transmission.<sup>49,50</sup> Subsequently, the time series for each sensor was demodulated and matched-filtered to achieve pulse compression. For all the numerical results presented in this paper, the received pressure time series consists of these matched-filtered demodulates.

During the experiment, the position of the VLA was tracked using a long-baseline acoustic navigation system consisting of four transponders deployed on the bottom and several interrogator hydrophones on the array. Navigation data was recorded immediately before and after each reception. Array positions for each of the ten four-period averages were determined by interpolating between the beginning and ending locations of the array.

In the results presented below, estimates of the noise level for each reception were used to determine plotting and detection thresholds. These estimates were obtained from spectral analysis of noise-only segments of data at the beginning and end of each reception. Further details of the noise analysis for the Hawaii VLA are discussed by Wage.<sup>51</sup>

## B. ATOC processing examples

The purpose of this section is to highlight important features of the short-time mode spectra by comparing the results for an ATOC reception with those for a simulated reception. Figure 13(a) is a plot of a demodulated pressure time series (one four-period average) recorded on the Hawaii array in late December 1995. Figure 13(b) shows the time series for a simulation of propagation over the Pioneer–Hawaii path. The simulation environment consists of Levitus background

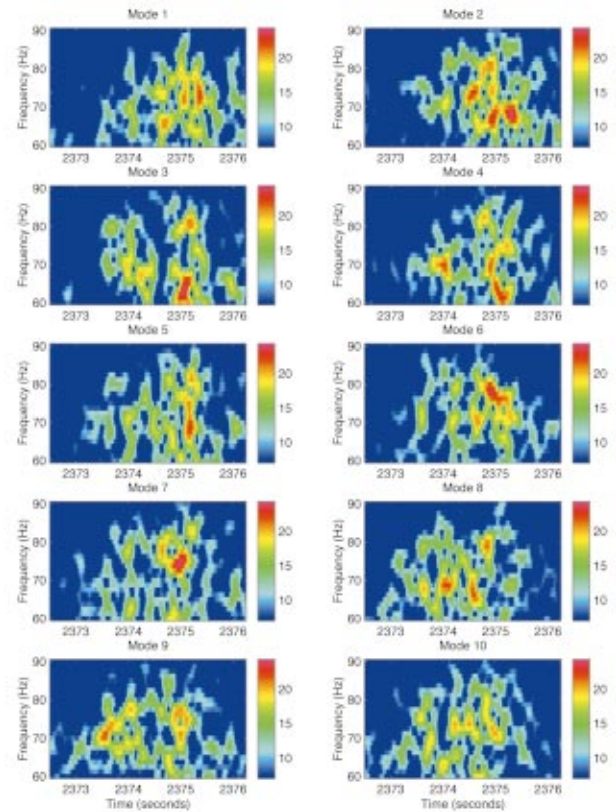


FIG. 14. Short-time Fourier mode estimates for the ATOC reception in Fig. 13(a). Color scale is in dB.

soundspeed profiles perturbed by  $\frac{1}{2}$  Garrett-Munk (GM) internal waves, as described in Sec. II. In the pressure time series plots, the 0-dB level corresponds to the estimated noise floor in the 75Hz bin (the center frequency). Since the simulation does not contain any additive noise components, it is assumed that there is a noise floor 12 dB below the peak in the pressure field, which is consistent with the ATOC measurements.

Based on Fig. 13, the experimental and simulated data are quite similar. Unlike the adiabatic example considered in Sec. IV D, there are no immediately identifiable modes contained in the late-arriving energy of either the measured or simulated reception. The most striking difference between the PE simulation and the real data is that the simulated reception has a sharp cutoff at 2375 s while the ATOC reception exhibits no discernible cutoff. Absence of a sharp cutoff in the ATOC data is attributed to interaction with the steep bottom slope near the Pioneer Seamount source, which the simulation does not model.<sup>51,52</sup>

The STFT processor for the measured and simulated receptions uses a pseudo-inverse filter for ten modes in conjunction with a 0.4-s lowpass filter (Hanning window), which has the required  $\pm 2.5$ -Hz bandwidth. Figure 14 shows the short-time Fourier mode estimates (as a function of time and frequency) for the first ten modes of the ATOC reception, and Fig. 15 shows the corresponding estimates for the first ten modes in the internal wave simulation. For modal time series plots the 0-dB level corresponds to the estimated noise level in mode 1 at 75 Hz for the reception.

There are a number of observations to make about the

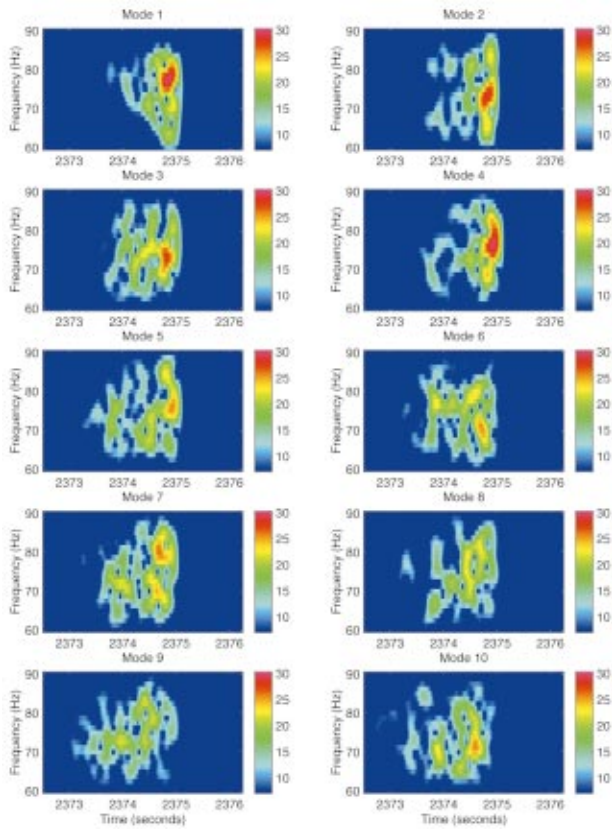


FIG. 15. Short-time Fourier mode estimates for the PE simulation with internal waves in Fig. 13(b). Color scale is in dB.

experimental results in Fig. 14. First, each mode consists of multiple arrivals, spread over 2–3 s. This is in stark contrast to the single, dispersive arrivals that characterized the adiabatic propagation example discussed in Sec. IV D. Second, note that the individual arrivals in each mode are on the order of 0.2 s wide, much wider than a typical ray arrival. This is due to the time-smearing inherent in the STFT processor, rather than to a fundamental difference between rays and modes. Third, recall that in the adiabatic case, the modes arrive in descending order and the highest modes are temporally separable from the lowest modes. For this ATOC reception, there is no obvious ordering of the arrivals and the spread of the signals is such that the first ten modes overlap in time. Fourth, the estimated modal time series contain faded arrivals. Frequency-selective fading occurs when two signals with different phase characteristics arrive simultaneously, i.e., within the time window used to compute the transform. Destructive interference of the signals results in deep fades of the spectral amplitude. If a short-time transform temporally resolves two signals, then only nonfaded arrivals (such as those found in the adiabatic example) are observed. The ATOC STFT processor begins to resolve signals at a separation of 0.2 s, thus the presence of faded arrivals in the Hawaii data suggests that the processor is measuring the interference pattern associated with multiple arrivals separated by less than 0.2 s.

A comparison of Figs. 14 and 15 indicates that the results of the  $\frac{1}{2}$  GM internal wave simulation qualitatively agree with the experimental data. Each of the time-varying

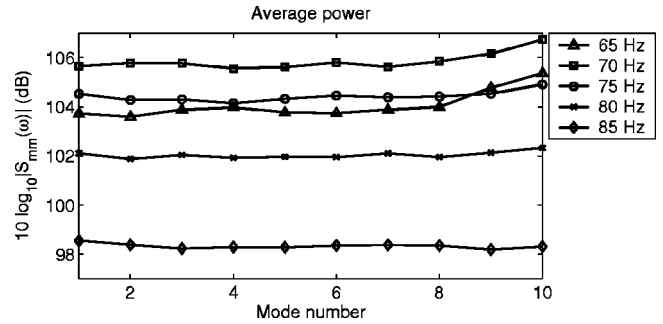


FIG. 16. Average power as a function of mode number in the 65-, 70-, 75-, 80-, and 85-Hz bins.

mode spectra for the PE simulation contains a series of faded arrivals. The sharp cutoff, which is a consequence of ignoring bathymetric effects near the source, is clearly evident in the mode estimates. Although the similarities between experiment and simulation are encouraging, the ATOC data does show significantly more time-spread than the PE data.

### C. Mode coherence

According to Dozier and Tappert,<sup>3,6</sup> internal-wave-induced scattering decorrelates the mode signals. In this section we examine the coherence of the first ten modes in the ATOC receptions using magnitude-squared coherence (MSC) as a metric. The MSC of two random processes is defined as<sup>53</sup>

$$\text{MSC}(\omega) = \frac{|S_{mn}(\omega)|^2}{S_{mm}(\omega)S_{nn}(\omega)}, \quad (16)$$

where  $S_{mn}$  is the cross power spectral density and  $S_{mm}$  and  $S_{nn}$  are the auto power spectral densities. In practice, the cross power spectrum is estimated by averaging over  $L$  measurements in each frequency bin, e.g., an estimate of the cross spectrum for modes  $m$  and  $n$  is

$$\hat{S}_{mn}(\omega) = \frac{1}{L} \sum_{l=1}^L \hat{a}_m(\omega, l) \hat{a}_n^*(\omega, l), \quad (17)$$

where  $\hat{a}_m$  and  $\hat{a}_n$  are the amplitude estimates for modes  $m$  and  $n$  and  $*$  denotes the complex conjugate. Setting  $m=n$  in Eq. (17) produces auto spectrum estimates. For the ATOC analysis, we obtain the measurements in each bin by subsampling the output of the STFT processor, taking one sample every 0.15 s. Since the processing window (i.e., the filter) is 0.4 s long, this subsampling corresponds to a 62.5% overlap between neighboring windows. To compute the spectral estimates, we use samples from a two-second interval (2373.4 to 2375.4) in each reception and average over all receptions.

Figure 16 shows the average power estimates ( $10 \log_{10} |\hat{S}_{mm}|$ ) as a function of mode number for the first ten modes in the 65-, 70-, 75-, 80-, and 85-Hz bins. Note that for these low modes the average power is approximately constant in each bin, which is consistent with Dozier and Tappert's prediction of an equipartitioning of energy among the modes. The slight increase for modes 9 and 10 at 65, 70, and 75 Hz is attributed to crosstalk from higher order modes

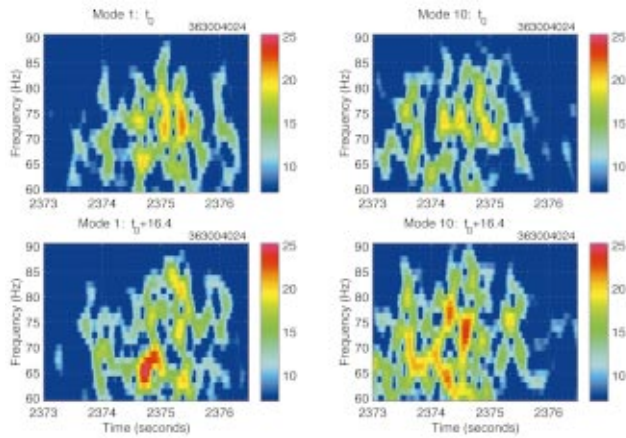


FIG. 17. Comparison of modes 1 and 10 for the first (top plots) and last (bottom plots) periods of a source transmission. Color scale is in dB.

not included in the estimate (recall the discussion of Fig. 7). Differences in absolute levels from bin to bin are a function of the source spectrum.

By definition, the MSC lies between 0 and 1. For the ATOC receptions, the maximum cross-mode coherence for any of the mode pairs in the 65-, 70-, 75-, 80-, and 85-Hz bins is 0.05. These experimental measurements indicate that the signals in the first ten modes are incoherent at a range of 3515 km. This result supports Dozier and Tappert's claim that modes decorrelate with range due to internal-wave effects.

#### D. Temporal variability

The purpose of this section is to examine the temporal variability of the mode arrivals at megameter range. For deep water environments, Colosi *et al.*<sup>54</sup> (citing the work of Flatte and Stoughton<sup>55</sup>) indicate that acoustic coherence times are on the order of tens of minutes, whereas the coherence times for internal waves are on the order of hours. In analyzing data from the ATOC Engineering Test (range=3250 km), Worcester *et al.* used 12.7-min coherent averages for the ray arrivals, since the SNR did not increase for longer averaging times.<sup>56</sup> For that same data set, Colosi *et al.* concluded that time fluctuations in the wavefronts show no coherence at 2-h lag times.<sup>54</sup> Note that in the long-range experiments cited above, the focus was primarily on analyzing the ray arrivals, rather than the late-arriving modes. The rest of this section considers the temporal variations of the mode arrivals in ATOC.

Recall that for each source transmission, the VLA recorded ten four-period averages of the 27.28-s pseudo-random sequence. The results discussed in Sec. V B were computed using the first four-period average of a transmission received by the Hawaii array in late December 1995. Figure 17 compares mode estimates for the first four-period average and the last four-period average of that transmission. The top plots are the estimated spectra for modes 1 and 10 from the first four periods and the bottom plots correspond to the last four periods. Note that the time difference between the end of the first reception and the start of the tenth is approximately 14.5 min. The plot clearly demonstrates that

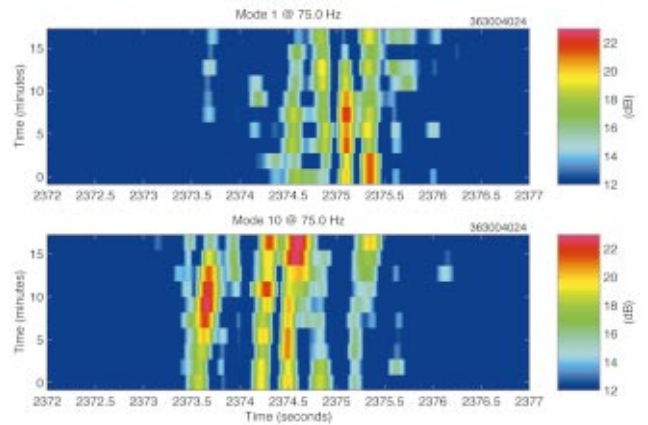


FIG. 18. Variability of modes 1 and 10 across a single transmission (18.2 min) in the 75-Hz bin.

the mode signals change significantly over that time interval: some arrivals drop out entirely, and new arrivals emerge. Using the center frequency bin, Fig. 18 provides a clearer picture of the temporal variability of the mode signals. The two plots in the figure are stacks of the received signals in mode 1 (top) and mode 10 (bottom) at successive 1.82-min (four-period) lags. While some of the peaks are consistent across the full transmission interval, others fade in/out suddenly.

There are a variety of ways to quantify the temporal variability of signals. In this paper, we consider two approaches. The first approach consists of computing the MSC between the first four-period average in a transmission and the successive four-period averages. Yang *et al.* used a similar method to analyze coherence times for a recent shallow water internal wave experiment.<sup>57</sup> Figure 19 shows the MSC estimate for mode 1, computed using the Hawaii VLA data. Each curve represents the mean over all transmissions. Note that the MSC decreases rapidly, reaching 0.5 at approximately 4.5 min and becoming effectively equal to zero for lag times greater than 14 min. The figure indicates a mild dependence on frequency: mode 1 at 85 Hz has a slightly shorter coherence time than mode 1 at 65 Hz. This apparent dependence may be an artifact due to the lower signal levels

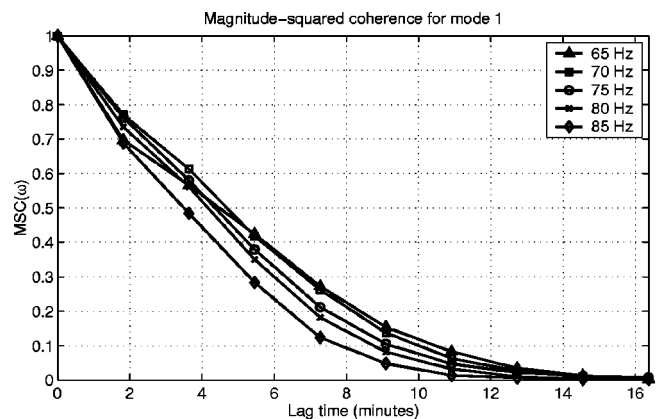


FIG. 19. Magnitude-squared coherence for mode 1 as a function of the lag time between the first four-period average and successive four-period averages in a single transmission. These curves depict the mean over all transmissions.

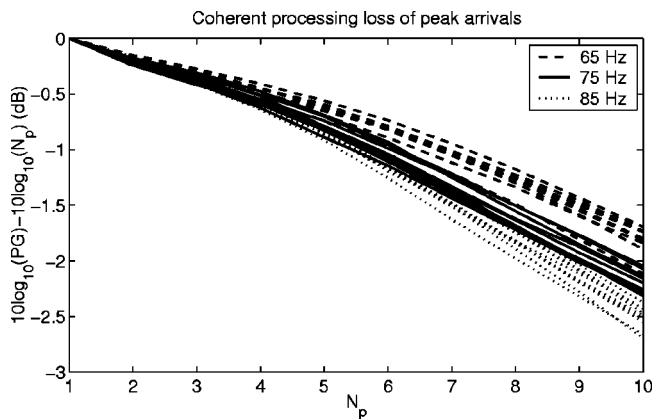


FIG. 20. Coherent processing loss for the peak arrivals in modes 1–10 for the 65-Hz, 75-Hz, and 85-Hz bins.

at the higher frequencies. The MSC estimates for mode 1 are representative of the results for modes 2–10.

The second approach to quantifying temporal variability focuses on the arrival peaks in the bandpass mode estimates. In previous work, Tang and Tappert used processing gain as a measure of the temporal coherence of pulses propagating through internal waves in a shallow (200 m) water environment at ranges of 20 km.<sup>58</sup> They studied pulse coherence times without addressing the issue of modes specifically. Processing gain is defined as a ratio of coherent to incoherent power. Consider the processing gain, PG, associated with a peak arrival in a mode:

$$PG = \frac{|\sum_{i=1}^{N_p} a(t_{\text{peak}}, i)|^2}{\sum_{i=1}^{N_p} |a(t_{\text{peak}}, i)|^2}, \quad (18)$$

where  $a(t_{\text{peak}}, i)$  is the estimated complex mode amplitude at time  $t_{\text{peak}}$  in the  $i$ th four-period average.  $N_p$  is the number of four-period averages included in the calculation. Note that the maximum value of PG is equal to  $N_p$  and is achieved when the signal is perfectly coherent. For the Hawaii data set, the following procedure is used to obtain an average processing gain for the peaks in each mode. The initial step consists of finding the peak arrival times for the first four-period average in each reception using a detection threshold of 12 dB above the estimated noise floor. Then the processing gain for each peak is calculated by computing the ratio of coherent and incoherent sums at the peak time. The number of periods ( $N_p$ ) to include in the sums varies from 1 to 10. The resulting gains are averaged over all peaks obtained for that mode in the Hawaii VLA data set (188 receptions). Figure 20 shows the coherent processing loss for the peaks, which is defined as  $10 \log_{10}(PG) - 10 \log_{10}(N_p)$ . This quantity measures how close the average processing gain is to the ideal gain achieved by a perfectly coherent signal. The dashed, solid, and dotted lines on the plot correspond to the average coherent processing loss for modes 1–10 at 65, 75, and 85 Hz, respectively. Recall that each four-period average represents 1.82 min of data. Based on the figure, processing gain is within 0.5 dB of the ideal gain for  $N_p$  up to 3. In other words the peaks are predominantly coherent up to 5.5 min. Beyond that, the average processing gain diverges from that of a perfectly coherent signal. Similar to the MSC estimates,

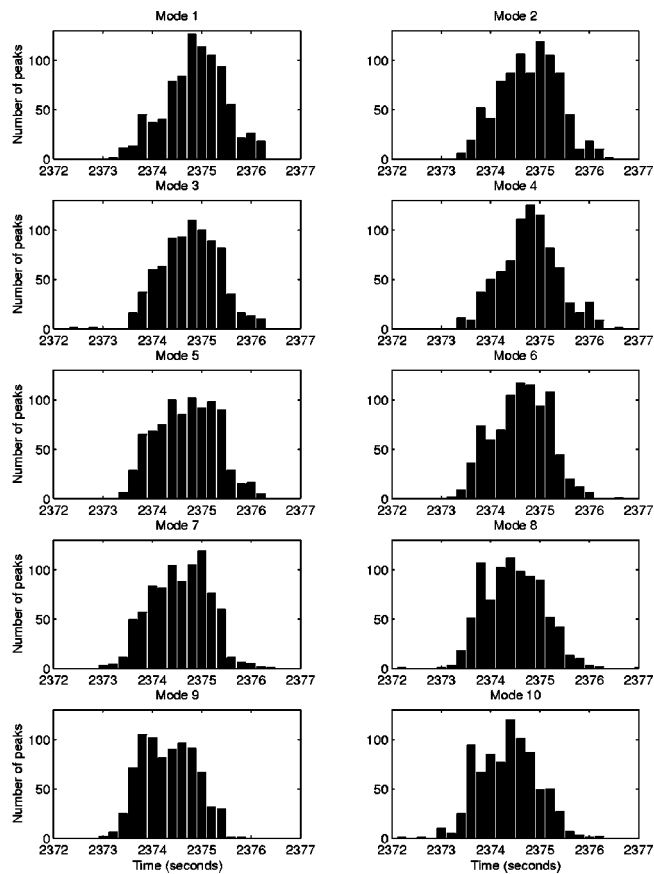


FIG. 21. Histogram of peak arrivals in the 75-Hz bin for the first ATOC reception group. Detection threshold was set at 12 dB above the estimated noise floor.

these curves indicate a mild dependence on frequency: modes at 65 Hz have slightly longer coherence times than the modes at 75 or 85 Hz. At a single frequency, there is no obvious ordering of the data by mode number. This is not surprising given the amount of mode coupling that occurs over the 3515-km propagation path.

It is important to note that Fig. 20 provides an average measure of temporal coherence. Based on the plot in Fig. 18, some of the mode arrivals are coherent over the reception period (18.2 min). Further analysis of the processing gain data reveals that approximately 9% of all arrivals are coherent over the entire reception (where coherence is defined to be  $PG > 9$ ).

## E. Arrival time statistics

On days that the ATOC source was operating, there were transmissions at 4-h intervals. Given the variability of the mode signals over a single 18.2-min reception, it is not surprising that the locations of the arrival peaks change substantially after 4 h. To get an idea of how the peak arrival times are distributed, consider the histograms for modes 1–10, shown in Fig. 21. These plots were compiled by picking peaks in the first group of ATOC receptions (year days 363–366, containing 200 four-period averages) using a detection threshold of 12 dB above the estimated noise floor for each mode. The results demonstrate that there is not a dominant arrival time in each mode; rather, the peaks are distributed

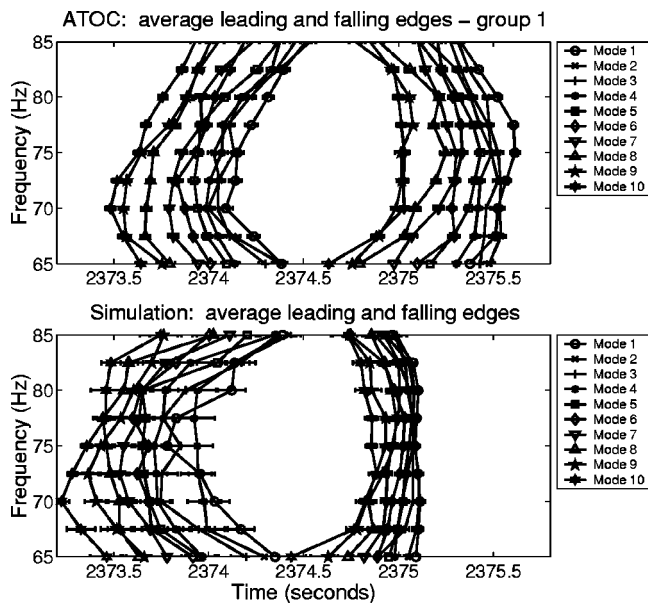


FIG. 22. Comparison of average leading and falling edges for the first group of ATOC receptions and a simulated data set. The latter includes ten simulated receptions through independent realizations of a  $\frac{1}{2}$  Garrett-Munk internal wave field.

between 2373 and 2376 s for all of the modes. Note that the distribution of the higher modes (e.g., mode 10) is skewed towards the early part of the 3-s interval while the low modes are concentrated towards the latter part of the interval. This is consistent with deep water dispersion, where higher modes arrive first.

Since there is not a dominant peak in each mode that can be tracked, it is necessary to consider average travel time statistics for the mode signals. For the ATOC data, the leading edge, falling edge, and centroid of the short-time Fourier mode estimates provide a useful characterization of the arrival structure. Leading and falling edges are defined as the first and last (respectively) time indices where the complex envelope of the mode estimate exceeds a threshold. The centroid is defined to be the center of mass of the portion of the complex envelope that is higher than the threshold value. For all of the results presented below, the threshold was set at 12 dB above the noise floor in each mode.

Figure 22 shows the results of averaging over all the receptions in the first group (a total of 200 four-period averages) to obtain the leading and falling edges as a function of frequency for the first 10 modes. For reference, the figure also includes the average leading and falling edges for the mode estimates of ten simulated receptions, which result from ten independent realizations of a  $\frac{1}{2}$  Garrett-Munk internal wave field. The error bars on these plots represent the standard error, i.e., the sample standard deviation divided by the square root of the number of samples included in the average.<sup>59</sup> The ATOC statistics reveal several significant features. First, the average spread between leading and falling edges is on the order of 1.5 s. Second, the high modes have earlier arrival times, while low modes have later arrival times, as would be expected in a deep water channel. Although there is some crossover between neighboring modes, the leading and falling edges show that there are statistically

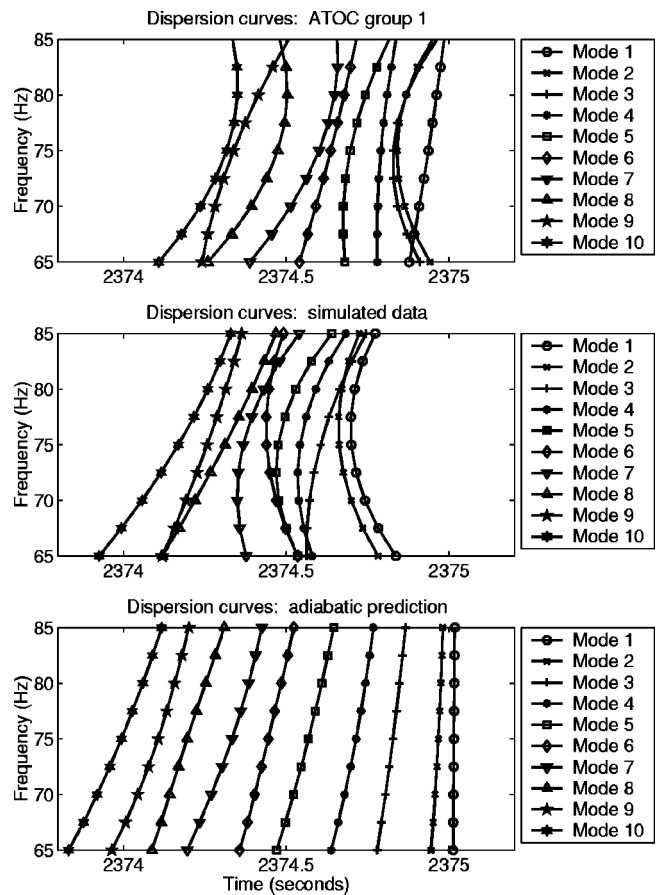


FIG. 23. Comparison of estimated dispersion curves for the first group of ATOC receptions, the simulated receptions, and the adiabatic predictions.

significant differences in arrival time among the modes, e.g., compare modes 1 and 10. Finally, the plot indicates that the signals at the center frequency (75 Hz) are more spread than those at either end of the band. This effect may be partially due to the fact that the same detection threshold is used for all frequency bins, while the source spectrum rolls off as a function of frequency.

Since the simulated data is averaged over only ten receptions, the resulting curves in Fig. 22 are not as smooth as the ATOC data and the error bars are larger. Nevertheless, the simulated data is comparable to the real data in two important respects: the leading edges show similar behavior (as a function of frequency) to the ATOC data, and the arrival times are also comparable. Unlike the falling edges in the ATOC data, however, the falling edges in the simulated data are much more concentrated. This sudden cutoff has been noted above and is likely the result of ignoring downslope propagation effects near the source.

A second-order least squares fit to the centroid data has been used to estimate average mode arrival times as a function of frequency, i.e., dispersion curves for each mode. Figure 23 compares the estimated dispersion curves for the first group of ATOC receptions with the dispersion curves obtained from the ten simulated receptions. Predicted adiabatic dispersion curves are included for reference. The experimental data shows the modes arriving in descending order (though there is some crossover among nearest neighbors). The simulated data show good agreement: the mean arrival

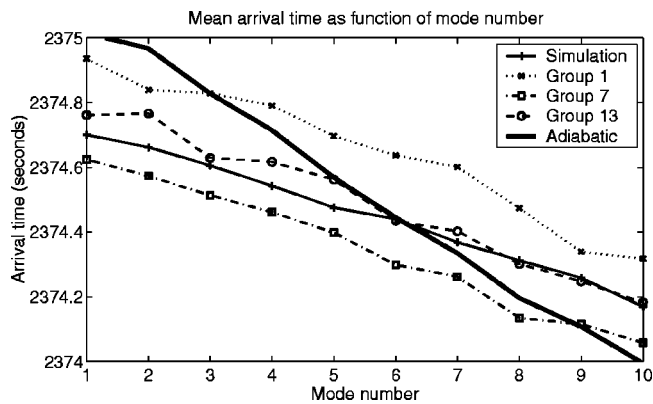


FIG. 24. Mean arrival time at 75 Hz as a function of mode number for several groups of ATOC receptions and a group of simulated receptions. An adiabatic prediction (heavy solid line) is included for reference.

times extend over the same interval, approximately 0.8 s. The key difference between the ATOC data and the simulated data in Fig. 23 is a shift in the mean arrival times: the curves for the first group of ATOC data occur approximately 0.2 s later than the centroids of the simulated receptions. Although Fig. 23 shows an obvious difference between experiment and simulation in the curvature of mode 1's dispersion characteristic, the plots for other ATOC reception groups indicate that this is not a consistent feature in the data. Comparing the ATOC and simulated data to the predicted adiabatic arrival times indicates that the intermode dispersion is larger for the adiabatic case than for the measured or simulated data, i.e., the difference in the mean arrival times of modes 1 and 10 is larger for the adiabatic prediction than for the estimated dispersion curves. This is expected because coupling of energy from mode to mode tends to drive the average arrival times closer together. Note that although the intermode dispersion is larger, the dispersion within each mode (intramode) is obviously smaller for the adiabatic case, as Figs. 2 and 3 demonstrate.

Figure 24 shows the mean arrival time at 75 Hz (obtained from the dispersion curves) as a function of mode number. There are five lines on the plot, which correspond to the results for ATOC reception groups 1, 7, and 13, the PE simulation result, and the adiabatic prediction. The standard errors<sup>58</sup> for the mean arrival time estimates range from 7 to 18 ms for the ATOC data and 18 to 32 ms for the simulated data. Figure 24 illustrates several important points. The trend of decreasing travel time with increasing mode number is obvious from all of the curves. The three ATOC groups shown represent the beginning, middle, and end of the Hawaii data set. It is clear that there are shifts in travel time over the course of the experiment, however the slope of the arrival time versus mode number curve remains roughly constant. Note that the slope of the line for the  $\frac{1}{2}$  Garrett-Munk PE simulation data also appears to agree with the experimental results. In contrast, the adiabatic mode prediction has a much steeper arrival-time versus mode number curve.

The Hawaii data set contains 5 months worth of data, taken between the end of December 1995 and May of 1996. Figure 25 illustrates how mean arrival time in the 75-Hz bin changes over the course of the experiment. Note that the

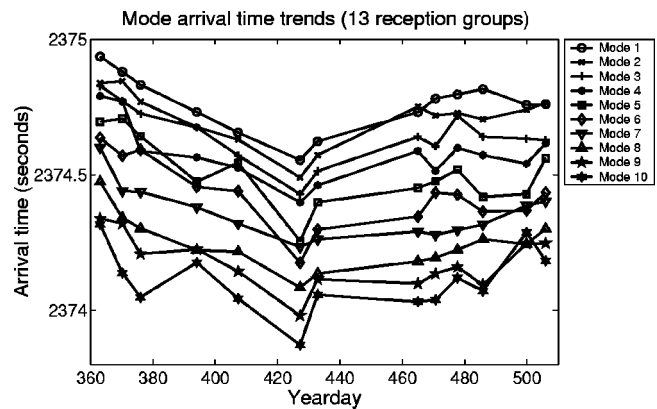


FIG. 25. Mean arrival time at 75 Hz for modes 1–10 as a function of yearday.

minimum travel time for all of the modes occurs around yearday 427, which corresponds to the beginning of March 1996. The trend of decreasing mode arrival time from the start of the experiment until March and increasing afterwards agrees with the trend observed in the ray arrivals for the Hawaii VLA.<sup>7</sup> The difference in the arrival times between the first group of receptions (yearday 363) and the sixth group of receptions (yearday 427) is between 0.3 and 0.5 s for the first ten modes. A *t*-test confirms that these time differences are statistically significant at the 1% level. Based on the 1998 *Science* article by the ATOC Consortium,<sup>7</sup> the ray arrivals exhibit somewhat smaller time shifts, on the order of 0.25 s over that same period. The *Science* article notes that the trend observed at the Hawaii array is not in agreement with the expected seasonal trend (which would have shown increasing travel times in winter and decreasing in the summer) and postulates that this is due to a subsurface warming near the receiver that offsets the winter surface cooling layer near the source.

## VI. CONCLUSION

In this paper we presented a short-time Fourier framework for broadband mode estimation. Using this flexible framework, we explored the time- and frequency-domain characteristics of the two most common modal beamforming algorithms and designed a mode processor for the ATOC experiment. Our analysis of five months of receptions at the Hawaii VLA produced a number of results regarding the mode arrival structure at megameter range. First, we demonstrated that the low mode signals at 3515 km consist of a series of arrivals, rather than the single dispersive arrival that typifies adiabatic propagation, confirming the predictions of numerous simulation studies. Second, we showed that the first ten modes have roughly equal average powers and that the cross-mode coherence is effectively zero. These results agree with Dozier and Tappert's conclusions based on theoretical and numerical work.<sup>3,6</sup> Third, we examined the temporal variability of the mode signals and determined that the average coherence times of the peaks in each bin are on the order of 5.5 min; coherence times of the overall signal (not just the peaks) are even shorter. Fourth, we computed centroid statistics that reveal mode-dependent trends in arrival

time and highlight mean shifts in the environment over 5 months of the experiment. We noted that the slope of the centroid arrival time versus mode number curve derived from the experimental data agrees with the slope derived from numerical simulations of propagation through  $\frac{1}{2}$  Garrett-Munk strength internal waves.

This research has important implications for acoustic tomography using normal modes. Noting that the individual mode arrivals are not stable over time, we conclude that inversions must be based on the statistics of the mode field. Additional work is needed to investigate the dependence of mode statistics on the background environment and the parameters of the internal wave field.

## ACKNOWLEDGMENTS

This work was supported in part by the Strategic Environmental Research and Development Program through Defense Advanced Research Projects Agency (DARPA) Grant No. MDA972-93-1-0003 and Office of Naval Research (ONR) Grant No. N00014-97-1-0788. K. Wage gratefully acknowledges additional support from an Armed Forces Communications and Electronics Association Postdoctoral Fellowship, and an ONR Ocean Acoustics Young Faculty Award. This paper is Woods Hole Oceanographic Institution contribution #10445. The authors thank the anonymous reviewers for their suggestions.

<sup>1</sup>W. Munk and C. Wunsch, "Ocean acoustic tomography: Rays and modes," *Rev. Geophys. Space Phys.* **21**(4), 777–793 (1983).  
<sup>2</sup>S. M. Flatte, R. Dashen, W. H. Munk, K. M. Watson, and F. Zachariassen, *Sound Transmission Through a Fluctuating Ocean* (Cambridge U. P., Cambridge, England, 1979).  
<sup>3</sup>L. B. Dozier and F. D. Tappert, "Statistics of normal mode amplitudes in a random ocean. I. Theory," *J. Acoust. Soc. Am.* **63**, 353–365 (1978).  
<sup>4</sup>E. Yu. Gorodetskaya, A. I. Malekhanov, A. G. Sazontov, and N. K. Vdovicheva, "Deep-Water Acoustic Coherence at Long Ranges: Theoretical Prediction and Effects on Large-Array Signal Processing," *IEEE J. Ocean. Eng.* **24**(2), 156–171 (1999).  
<sup>5</sup>J. A. Colosi and S. M. Flatte, "Mode coupling by internal waves for multimegahertz acoustic propagation in the ocean," *J. Acoust. Soc. Am.* **100**, 3607–3620 (1996).  
<sup>6</sup>L. B. Dozier and F. D. Tappert, "Statistics of normal mode amplitudes in a random ocean. II. Computations," *J. Acoust. Soc. Am.* **64**, 533–547 (1978).  
<sup>7</sup>The ATOC Consortium, "Ocean Climate Change: Comparison of Acoustic Tomography, Satellite Altimetry, and Modeling," *Science* **281**, 1327–1332 (1998).  
<sup>8</sup>L. M. Brekhovskikh and Yu. P. Lysanov, *Fundamentals of Ocean Acoustics*, 2nd ed. (Springer-Verlag, New York, 1991).  
<sup>9</sup>Y. Desaubies, "A uniformly valid solution for acoustic normal mode propagation in a range varying ocean," *J. Acoust. Soc. Am.* **76**, 624–626 (1984).  
<sup>10</sup>Y. Desaubies, C. S. Chiu, and J. H. Miller, "Acoustic mode propagation in a range-dependent ocean," *J. Acoust. Soc. Am.* **80**, 1148–1160 (1986).  
<sup>11</sup>S. Levitus and T. P. Boyer, *World Ocean Atlas 1994 Volume 4: Temperature*, 1994, NOAA Atlas NESDIS 4.  
<sup>12</sup>S. Levitus, R. Burgett, and T. P. Boyer, *World Ocean Atlas 1994 Volume 3: Salinity*, NOAA Atlas NESDIS 3, 1994.  
<sup>13</sup>NOAA, National Geophysical Data Center, Boulder, CO, Data Announcement 88-MGG-02, *Digital relief of the Surface of the Earth*, 1988.  
<sup>14</sup>The environment contains the actual bathymetry along the path, with the exception of one simplification: the steep downslope near the source has been eliminated. In the simulations the source is at 939.5-m depth (the depth of the actual seamount), and the bottom depth at the source is 3317 m. The effects of the near-source downslope propagation are discussed briefly in Sec. V B of this paper and by Wage.<sup>51</sup>

<sup>15</sup>M. D. Collins, *User's Guide for RAM*, Naval Research Laboratory, Washington, DC.  
<sup>16</sup>J. A. Colosi and M. G. Brown, "Efficient numerical simulation of stochastic internal-wave-induced sound-speed perturbation fields," *J. Acoust. Soc. Am.* **103**, 2232–2235 (1998).  
<sup>17</sup>J. A. Colosi, S. M. Flatte, and C. Bracher, "Internal-wave effects on 1000-km oceanic acoustic pulse propagation: Simulation and comparison with experiment," *J. Acoust. Soc. Am.* **96**, 452–468 (1994).  
<sup>18</sup>J. A. Colosi and the ATOC Group, "A Review of Recent Results on Ocean Acoustic Wave Propagation in Random Media: Basin Scales," *IEEE J. Ocean. Eng.* **24**(2), 138–155 (1999).  
<sup>19</sup>A. G. Sazontov and V. A. Farfel, "Matched filtering of a narrowband pulse signal transmitted through a random waveguide channel," *Sov. Phys. Acoust.* **38**(6), 591–595 (1992).  
<sup>20</sup>E. Yu. Gorodetskaya, A. I. Malekhanov, A. G. Sazontov, and V. A. Farfel, "Effects of Long-Range Propagation of Sound in a Random Inhomogeneous Ocean on the Gain Loss of a Horizontal Antenna Array," *Acoust. Phys.* **42**(5), 543–549 (1996).  
<sup>21</sup>A. G. Sazontov, and V. A. Farfel, "Fluctuation characteristics of the response of a horizontal array in a randomly inhomogeneous ocean with short-time averaging," *Sov. Phys. Acoust.* **37**(5), 514–518 (1991).  
<sup>22</sup>N. K. Vdovicheva, E. Yu. Gorodetskaya, A. I. Malekhanov, and A. G. Sazontov, "Gain of a Vertical Antenna Array in a Randomly Inhomogeneous Oceanic Waveguide," *Acoust. Phys.* **43**(6), 669–675 (1997).  
<sup>23</sup>A. G. Sazontov "Quasiclassical solution of the radiation transport equation in a scattering medium with regular refraction," *Acoust. Phys.* **42**(4), 487–494 (1996).  
<sup>24</sup>M. G. Brown, J. Viechnicki, and F. D. Tappert, "On the measurement of modal group time delays in the deep ocean," *J. Acoust. Soc. Am.* **100**, 2093–2102 (1996).  
<sup>25</sup>W. Menke, *Geophysical Data Analysis: Discrete Inverse Theory* (Academic, New York, 1989).  
<sup>26</sup>H. L. Van Trees, *Detection, Estimation, and Modulation Theory, Part I* (Wiley, New York, 1968).  
<sup>27</sup>J. R. Buck, J. C. Preisig, and K. E. Wage, "A unified framework for mode filtering and the maximum *a posteriori* mode filter," *J. Acoust. Soc. Am.* **103**, 1813–1824 (1998).  
<sup>28</sup>R. H. Ferris, "Comparison of measured and calculated normal-mode amplitude functions for acoustic waves in shallow water," *J. Acoust. Soc. Am.* **52**, 981–988 (1972).  
<sup>29</sup>F. Ingenito, "Measurements of mode attenuation coefficients in shallow water," *J. Acoust. Soc. Am.* **53**, 858–863 (1973).  
<sup>30</sup>C. T. Tindle, K. M. Guthrie, G. E. J. Bold, M. D. Johns, D. Jones, K. O. Dixon, and T. G. Birdsall, "Measurements of the frequency dependence of normal modes," *J. Acoust. Soc. Am.* **64**, 1178–1185 (1978).  
<sup>31</sup>R. H. Headrick, J. F. Lynch, J. N. Kemp, A. E. Newhall, K. von der Heydt, J. Apel, M. Badiey, C. S. Chiu, S. Finette, M. Orr, B. Pasewark, L. Turgot, S. Wolf, and D. Tielbuerger, "Acoustic normal mode fluctuation statistics in the 1995 swarm internal wave scattering experiment," *J. Acoust. Soc. Am.* **107**, 201–220 (2000).  
<sup>32</sup>P. Casey, "Mode Extraction for Long Range Underwater Acoustic Signals," M. S. thesis, University of Auckland, February 1995.  
<sup>33</sup>C. S. Chiu, C. W. Miller, and J. F. Lynch, "Optimal Modal Beamforming of Bandpass Signals Using an Undersized Sparse Vertical Hydrophone Array: Theory and a Shallow-Water Experiment," *IEEE J. Ocean. Eng.* **22**(3), 522–533 (1997).  
<sup>34</sup>T. C. Yang, "Broadband source localization and signature estimation," *J. Acoust. Soc. Am.* **93**, 1797–1806 (1993).  
<sup>35</sup>P. Sutton, W. M. L. Morawitz, B. D. Cornuelle, G. Masters, and P. F. Worcester, "Incorporation of acoustic normal mode data into tomographic inversions in the Greenland Sea," *J. Phys. Oceanogr.* **99**(C6), 12487–12502 (1994).  
<sup>36</sup>K. D. Heaney and W. A. Kuperman, "Very long-range source localization with a small vertical array," *J. Acoust. Soc. Am.* **104**, 2149–2159 (1998).  
<sup>37</sup>H.-Y. Chen and I.-T. Lu, "Localization of a broadband source using a matched-mode procedure in the time-frequency domain," *IEEE J. Ocean. Eng.* **19**(2), 166–174 (1994).  
<sup>38</sup>J. B. Allen and L. R. Rabiner, "A Unified Approach to Short-Time Fourier Analysis and Synthesis," *Proc. IEEE* **65**(11), 1558–1564 (1977).  
<sup>39</sup>S. H. Nawab and T. F. Quatieri, "Short-Time Fourier Transform," in *Advanced Topics in Signal Processing* (Prentice Hall, Englewood Cliffs, NJ, 1988), pp. 289–337.  
<sup>40</sup>Note that the block diagram in Fig. 5 implicitly assumes that the array is vertical. When the array is tilted, the processor must incorporate some sensor-dependent timing corrections as discussed by Wage.<sup>51</sup>

- <sup>41</sup>F. J. Harris, "On the Use of Windows for Harmonic Analysis with the Discrete Fourier Transform," *Proc. IEEE* **66**(1), 51–83 (1978).
- <sup>42</sup>H. Cox, R. M. Zeskind, and M. M. Owen, "Robust adaptive beamforming," *IEEE Trans. Acoust., Speech, Signal Process.* **ASSP-35**(10), 1365–1376 (1987).
- <sup>43</sup>G. Strang, *Linear Algebra and Its Applications*, 3rd ed. (Harcourt Brace Jovanovich, San Diego, CA, 1988).
- <sup>44</sup>A. G. Voronovich, V. V. Goncharov, A. Yu. Nikol'tsev, and Yu. A. Chepurin, "Comparative analysis of methods for the normal mode decomposition of a sound field in a waveguide: numerical simulation and full-scale experiment," *Sov. Phys. Acoust.* **38**(4), 365–370 (1992).
- <sup>45</sup>T. C. Yang, "A method of range and depth estimation by modal decomposition," *J. Acoust. Soc. Am.* **82**, 1736–1745 (1987).
- <sup>46</sup>Higher-order modes are propagating in the waveguide, but their arrivals occur prior to the start-time of the simulation window.
- <sup>47</sup>Unlike the simulation in Fig. 2, mode 1 is excited by the source in this example.
- <sup>48</sup>The ATOC Instrumentation Group: B. M. Howe, S. G. Anderson, A. Baggeroer, J. A. Colosi, K. R. Hardy, D. Horwitt, F. W. Karig, S. Leach, J. A. Mercer, Jr., K. Metzger, L. O. Olson, D. A. Peckham, D. A. Reddaway, R. R. Ryan, R. P. Stein, K. von der Heydt, J. D. Watson, S.-L. Weslander, and P. F. Worcester, "Instrumentation for the Acoustic Thermometry of Ocean Climate (ATOC) Prototype Pacific Ocean Network," in *OCEANS '95 Conference Proceedings*, San Diego, CA, October 1995, pp. 1483–1500.
- <sup>49</sup>Although the source transmitted 44 periods of the M-sequence, the array only recorded 40 periods. The start-time for recording was chosen so that sampling began approximately two periods after the start of the reception.<sup>50</sup>
- <sup>50</sup>P. Worcester, "ATOC95: Autonomous Vertical Line Arrays Experiment Plan," 1995.
- <sup>51</sup>K. E. Wage, "Broadband Modal Coherence and Beamforming at Megameter Ranges," Ph.D. thesis, Massachusetts Institute of Technology/Woods Hole Oceanographic Institution, February 2000.
- <sup>52</sup>K. D. Heaney, "Inverting for Source Location and Internal Wave Strength Using Long Range Ocean Acoustic Signals," Ph.D. thesis, University of California San Diego, 1997.
- <sup>53</sup>G. C. Carter, "Tutorial overview of coherence and time delay estimation," in *Coherence and Time Delay Estimation*, edited by G. Clifford Carter (IEEE, New York, 1993), pp. 1–27.
- <sup>54</sup>J. A. Colosi, E. K. Scheer, S. M. Flatte, B. D. Cornuelle, M. A. Dzieciuch, P. F. Worcester, B. M. Howe, J. A. Mercer, R. C. Spindel, K. Metzger, T. G. Birdsall, and A. B. Baggeroer, "Comparisons of measured and predicted acoustic fluctuations for a 3250-km propagation experiment in the eastern North Pacific Ocean," *J. Acoust. Soc. Am.* **105**, 3202–3218 (1999).
- <sup>55</sup>S. M. Flatte and R. B. Stoughton, "Predictions of internal-wave effects on ocean acoustic coherence, travel-time variance, and intensity moments for very long-range propagation," *J. Acoust. Soc. Am.* **84**, 1414–1424 (1988).
- <sup>56</sup>P. F. Worcester, B. D. Cornuelle, M. A. Dzieciuch, W. H. Munk, B. M. Höwe, J. A. Mercer, R. C. Spindel, J. A. Colosi, K. Metzger, T. G. Birdsall, and A. B. Baggeroer, "A test of basin-scale acoustic thermometry using a large-aperture vertical array at 3250-km range in the eastern North Pacific Ocean," *J. Acoust. Soc. Am.* **105**, 3185–3201 (1999).
- <sup>57</sup>T. C. Yang, K. Yoo, and M. Siderius, "Internal waves and its effect on signal propagation on the Adventure Bank," in *Proceedings of the 8th International Congress on Sound and Vibration*, Hong Kong, July 2001, pp. 3001–3008.
- <sup>58</sup>X. Tang and F. D. Tappert, "Effects of internal waves on sound pulse propagation in the Straits of Florida," *IEEE J. Ocean. Eng.* **22**(2), 245–255 (1997).
- <sup>59</sup>S. A. Teukolsky, W. H. Press, W. T. Vetterling, and B. P. Flannery, *Numerical Recipes in Fortran* (Cambridge U.P., Cambridge, 1992), Chap. 14, p. 610.